

blob loss: instance imbalance aware loss functions for semantic segmentation

Florian Kofler^{1,2,3}, Suprosanna Shit^{1,2}, Ivan Ezhov^{1,2}, Lucas Fidon⁴, Izabela Horvath^{1,5}, Rami Al-Maskari^{1,5}, Hongwei Li^{1,13}, Harsharan Bhatia^{5,6}, Timo Loehr^{1,3}, Marie Piraud⁷, Ali Erturk^{5,6,8,9}, Jan Kirschke³, Jan Peeken^{9,10,11,12}, Tom Vercauteren⁴, Claus Zimmer³, Benedikt Wiestler³ ^{*}, and Bjoern Menze^{1,13}^{*}

¹ Department of Informatics, Technical University Munich, Germany

² TranslaTUM - Central Institute for Translational Cancer Research, Technical University of Munich, Germany

³ Department of Diagnostic and Interventional Neuroradiology, School of Medicine, Klinikum rechts der Isar, Technical University of Munich, Germany

⁴ School of Biomedical Engineering & Imaging Sciences, King's College London, United Kingdom

⁵ Institute for Tissue Engineering and Regenerative Medicine, Helmholtz Institute Munich (iTERM), Germany

⁶ Institute for Stroke and dementia research (ISD), University Hospital, LMU Munich, Germany

⁷ Helmholtz AI, Helmholtz Zentrum München, Germany

⁸ Graduate school of neuroscience (GSN), Munich, Germany

⁹ Munich cluster for systems neurology (Synergy), Munich, Germany

¹⁰ Department of Radiation Oncology, Klinikum rechts der Isar, Technical University of Munich, Germany

¹¹ Institute of Radiation Medicine (IRM), Department of Radiation Sciences (DRS), Helmholtz Zentrum, Munich, Germany

¹² Deutsches Konsortium für Translationale Krebsforschung (DKTK), Partner Site Munich, Germany

¹³ Department of Quantitative Biomedicine, University of Zurich, Switzerland

Abstract. Deep convolutional neural networks (CNN) have proven to be remarkably effective in semantic segmentation tasks. Most popular loss functions were introduced targeting improved volumetric scores, such as the Sørensen–Dice coefficient (DSC). By design, DSC can tackle class imbalance; however, it does not recognize instance imbalance within a class. As a result, a large foreground instance can dominate minor instances and still produce a satisfactory DSC. Nevertheless, missing out on instances will lead to poor detection performance. This represents a critical issue in applications such as disease progression monitoring. For example, it is imperative to locate and surveil small-scale lesions in the follow-up of multiple sclerosis patients.

We propose a novel family of loss functions, nicknamed *blob loss*, primarily aimed at maximizing instance-level detection metrics, such as *F1*

^{*} contributed equally as senior authors

score and *sensitivity*. *Blob loss* is designed for semantic segmentation problems in which the instances are the connected components within a class. We extensively evaluate a DSC-based *blob loss* in five complex 3D semantic segmentation tasks featuring pronounced instance heterogeneity in terms of texture and morphology. Compared to soft Dice loss, we achieve 5% improvement for MS lesions, 3% improvement for liver tumor, and an average 2% improvement for Microscopy segmentation tasks considering *F1* score.

Keywords: semantic segmentation loss function, instance imbalance awareness, multiple sclerosis, lightsheet microscopy

1 Introduction

In recent years convolutional neural networks (CNN) have gained increasing popularity for complex machine learning tasks, such as semantic segmentation. A plethora of loss functions for model training evaluate on and promise to optimize global volumetric metrics, such as Dice coefficient (DSC) [6, 17, 18, 23, 28]. However, as shown in multiple previous studies *DSC* is sub-optimal in cases where the object of interest is heavily heterogeneous in terms of topology [25] or class-imbalance [2, 9, 21, 28]. Additionally, established metrics have been shown to correlate insufficiently with expert assessment [15].

In many segmentation tasks, instances do not overlap in the image and, therefore, can be defined as connected components. Further, many of those tasks face relevant instance imbalance, where large foreground connected components dominate over smaller ones within a class, as illustrated in Figure 1. This is not adequately reflected in terms of *DSC*. Instances can vary not only with regard to size but also texture and other morphological features. Instance imbalance is particularly pronounced and significant in medical applications: For example, even a single new multiple sclerosis (MS) lesion can impact the therapy decision. Despite many ways to compensate for class imbalance, there is a notable void in addressing instance imbalance.

Related work: Sirinukunwattana et al. [27] suggested an instance-based Dice metric for evaluating segmentation performance. Salehi et al. [23] were among the first to propose a loss function, called *Tversky loss*, for semantic segmentation of multiple sclerosis lesions in magnetic resonance imaging (MR), trying to improve detection metrics. Similarly, Zhu et al. [32] introduced Focal Loss, initially designed for object detection tasks [16], into medical semantic segmentation tasks.

There have been few recent attempts aiming for a solution to instance imbalance. Zhang et al. [30] propose an auxiliary lesion-level sphere prediction task. However, they do not explicitly consider each instance separately. Shirokikh et al. [24] propose an instance weighted loss function where a global weight map is inversely proportional to the size of the instances. However, unlike size, not

all types of imbalance, such as morphology or texture, can be quantified easily, limiting the method’s applicability.

Contribution: We propose *blob loss*, a method to convert any loss function into a novel instance imbalance aware loss function for semantic segmentation problems designed to optimize detection metrics. We evaluate its performance on five complex three-dimensional (3D) semantic segmentation tasks, for which the discovery of miniature structures matters. We demonstrate that extending soft Dice loss to a *blob loss* can help to improve detection performance in these multi-instance semantic segmentation tasks significantly. Furthermore, we also achieve volumetric improvements in some cases.

2 Methods

First, we introduce the problem of instance imbalance in semantic segmentation tasks. Then we present our proposed *blob loss* functions. Last we describe the experimental setup for evaluation.

2.1 Problem Statement

By definition of established volumetric metrics (or losses), large foreground areas can dominate the final value, see Figure 1. This is because the volumetric measures only accumulate true or false predictions on a voxel level but not at the instance level. Therefore, training models with volumetry-based loss functions, such as soft Dice loss (*dice*), often leads to unsatisfactory instance detection performance. To achieve a better detection performance, it is necessary to take instance imbalance into account. Instance imbalance can be of many categories, such as morphology and texture. Importantly, instance imbalance often cannot be easily specified and quantified for use in CNN training, for example, as instance weights in the loss function. Thus, using conventional methods, it is difficult to incorporate instance imbalance in CNN training. Therefore, we aim to design loss functions to compensate for the instance imbalance while being agnostic to the instance imbalance type.

2.2 *blob loss* Formulation

Consider a binary segmentation with N instances. Instances are defined as the connected components of the foreground. Now, for different input images, N can vary from few to many, as illustrated in Figure 4. Traditionally, instance segmentation algorithms predict each object separately and then tackle semantic segmentation. Building a pipeline involving cascaded CNNs for object detection and segmentation is a cumbersome process and often leads to poor segmentation performance [5]. Further, our case is a simplified problem where instances can be recovered from connected component analysis of the network predictions. This leads us to address instance imbalance within a binary semantic segmentation framework. At the same time, we remain agnostic towards particular instance

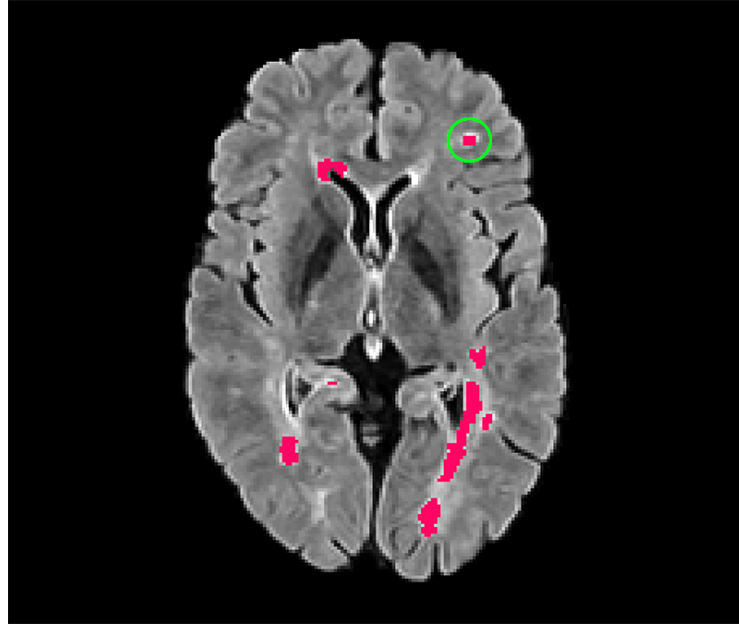


Fig. 1. Problem statement: The Sørensen–Dice coefficient (DSC) for the segmentation with vs. without lesion n , encircled in green, is: 0.9806. Therefore, the segmentations are hardly distinguishable in terms of DSC. However, from a clinical perspective the difference is important as detection of a single lesion can affect treatment decisions. Consequently, training neural networks with soft Dice loss often leads to unsatisfactory results, compare Figures 5 and 6.

attributes and do not incorporate these in the loss function. To this extent, we propose to leverage the existing ground truth annotations and formally propose a novel family of instance-aware loss functions. Specifically, we mask all but one instance for each of the present instances to compute our loss. Finally, we average them over all instances. Thus we assign equal importance to all instances irrespective of their size, shape, texture, and other topological attributes.

We propose to convert any loss function \mathcal{L} for binary semantic segmentation into an instance-aware loss function \mathcal{L}_{blob} defined as:

$$\mathcal{L}_{blob}((p_i)_{i \in \Omega}, (g_i)_{i \in \Omega}) = \frac{1}{N} \sum_{n=1}^N \mathcal{L}((p_i)_{i \in \Omega_n}, (g_i)_{i \in \Omega_n}) \quad (1)$$

where Ω is the image domain, $\{g_i\}_{i \in \Omega}$ is the ground-truth segmentation, $\{p_i\}_{i \in \Omega}$ is the predicted segmentation, N is the number of instances in the foreground, and, for the n^{th} instance, Ω_n is the image domain after excluding the foreground voxels belonging to all the other instances. It is worth noting that the background voxels are included in every Ω_n . This masking process is illustrated by Figure 2.

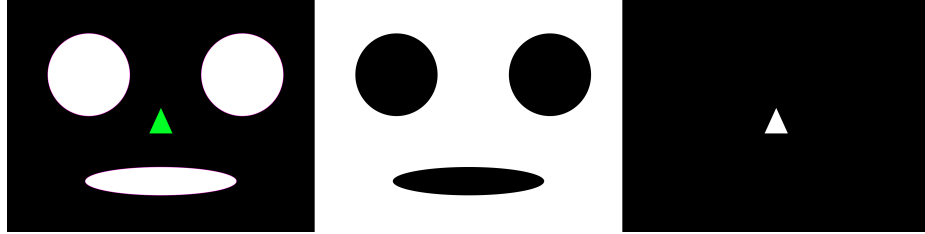


Fig. 2. Masking process described in Equation (1). Left: the global ground truth label (GT), with the n^{th} component highlighted in green. Middle: The loss mask Ω_n for the n^{th} component (MASK) for multiplication with the network outputs. Right: the label used for the computation of the local *blob loss* for the n^{th} component. This process is repeated for every component.

To compute the total loss for a volume, we combine the instance-wise Loss component from Equation (1) with a global component to obtain the final Loss:

$$\mathcal{L} = \alpha \mathcal{L}_{global} + \beta \mathcal{L}_{blob} \quad (2)$$

where α and β denote the weights for the global and instance constraint \mathcal{L}_{blob} .

2.3 blob loss Implementation

We provide a sample Pytorch implementation of a *dice*-based *blob loss* on GitHub.

In order to accelerate our trainings, we precompute the instances, here defined as connected components using *cc3d* [26], version 3.2.1.

We propose hyperparameters $\alpha = 2.0$ and $\beta = 1.0$ as starting point fine-tuning *blob loss* to a segmentation problem.

2.4 Model training

Basic U-Net: For all our experiments, we use a basic 3D U-Net implemented via MONAI inspired by [8] and further depicted in supplemental materials. Furthermore, we use a dropout ratio of 0.1 and employ *mish* as activation function [19]. Otherwise, we stick to the default parameters of the U-Net implementation.

Loss Functions for Comparison As baselines we use the MONAI implementations of soft Dice loss (*dice*) and Tversky loss (*tversky*) [23]. For *tversky*, we always use the standard parameters of $\alpha = 0.3$ and $\beta = 0.7$ suggested by the authors in the original publication [23]. For comparison we create *blob dice*, by transforming the standard *dice* into a *blob loss* using our conversion method Equation (1). The final loss is obtained by employing *dice* in the \mathcal{L}_{global} and \mathcal{L}_{blob} terms of the proposed total loss Equation (2). In analog fashion, we derive

blob tversky. Furthermore, we compare against *inverse weighting (iw)*, the globally weighted loss function of Shirokikh et al. [24]. For this, we use the official GitHub implementation to compute the weight maps and loss and deploy these in our training pipelines.

Training Procedure: Our CNNs are trained on multiple cuboid-shaped crops per batch element, with higher resolution in the axial dimension, enabling the learning of contextual image features. The crops are randomly sampled around a center voxel that consists of *foreground* with a 95% probability. We consider one epoch as one full iteration of forward and backward passes through all batches of the training set. For all training, *Ranger21* [29] serves as our optimizer. For each experiment, we keep the initial learning rate (lr) constant between training runs. Depending on the segmentation task, we deploy varying suitable image normalization strategies. For comparability, we keep all training parameters except for the loss functions constant on a segmentation task basis and stick to this standard training procedure.

Training-Test Split and Model Selection: Given the high heterogeneity of our bio-medical datasets and the limited availability of high-quality ground truth annotations due to the very costly labeling procedures requiring domain experts, we do not set aside data for validation, and therefore do not conduct model selection. Instead, inspired by [13], we split our data 80:20 into training and test set and evaluate on the last checkpoint of the model training. As an exception, the MS dataset comes with predefined training, validation, and test set splits; therefore, we additionally evaluate the *best* model checkpoint, meaning the model with the lowest loss on the validation set. As we are more interested in *blob loss*' generalization capabilities than exact quantification of improvements on particular datasets, we prioritize a broad validation on multiple datasets over cross-validation.

Inference and Test Time Augmentations: We compute our binary segmentation maps using a threshold of 0.5 after deriving the network outputs through a sliding window inference. To obtain more robust results, we employ test-time augmentations, namely spatial flips and subtle random Gaussian noise, for a total of 13 variations of the original input data.

Technical Details: Our experiments were conducted using NVIDIA RTX8000, RTX6000, RTX3090, and A6000 GPUs using CUDA version 11.4 in conjunction with Pytorch version 1.9.1 and MONAI version 0.7.0.

2.5 Evaluation Metrics and Interpretation

Metrics: We obtain global, volumetric performance measures from *pymia* [14]. In addition to DSC, we also evaluate *volumetric sensitivity (S)*, *volumetric precision (P)*, and the *Surface Dice similarity coefficient (SDSC)*. For instance-wise

detection metrics, we employ a proven evaluation pipeline from Pan et al. [20]. We compute, namely instance F1 ($F1$), *instance sensitivity (IS)* and *instance precision (IP)*. The metric computations are based on *true positive (TP)*, *false positive (FP)*, and *false negative (FN)* instances defined in 3D space as follows: if a predicted ‘blob’ has an overlap of at least *one* voxel with a ground truth label, it is considered a True Positive. Otherwise, it is regarded as a False Positive. Ground truth structures with no overlap are counted as False Negatives. Based on these values, we can compute instance sensitivity as $S = TP/(TP + FN)$, instance precision as $P = TP/(TP + FP)$, and instance ($F1$) score as $2 * (S * P)/(S + P)$.

Interpretation: By design, human annotators tend to overlook tiny structures. For comparison, human annotators initially missed 29% of micrometastases when labeling the DeepMACT light-sheet microscopy dataset [20]. Therefore,

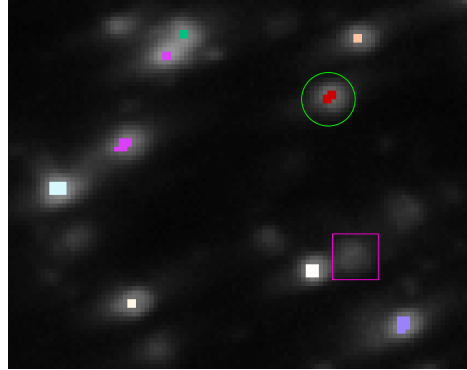


Fig. 3. Zoomed in 2D view on a volume of the SHANEL [31] dataset. The overlayed labels are colored according to a 3D connected component analysis. The expert biologists did not label each foreground object in every slice; e.g. the magenta-colored square. Furthermore, the contours of the structures are imperfectly segmented, for instance, the red label within the bright green circle. These effects can partially attributed to the ambiguity of the light-sheet microscopy signal. However, they are also observed in the human annotations of the MS and LiTS dataset.

the likelihood of a structure being correctly labeled in the ground truth is much higher for foreground than for background structures. Additionally, human annotators have a tendency to label a structure’s center but do not perfectly trace its contours. Both phenomena are illustrated in Figure 3. These effects are particularly pronounced for the microscopy datasets, which often feature thousands of blobs. These factors are important to keep in mind when interpreting the results. Consequently, volumetric and instance sensitivity are much more informative than volumetric and instance precision.

3 Experiments

To validate *blob loss*, we train segmentation models on a selection of datasets from different 3D imaging modalities, namely brain MR, thorax CT, and light-sheet microscopy. We select datasets featuring a variety of fragmented blob segmentation problems. Figure 4 features an overview over blob counts, volumetrics, and shape features in the datasets. For simplicity we use the default values $\alpha = 2.0$ and $\beta = 1.0$ across all experiments.

3.1 Multiple Sclerosis (MR)

Dataset & Segmentation Task:

The Multiple Sclerosis (MS) dataset, comprising 521 single timepoint MR examinations of patients with MS, was collected for internal validation of MS lesion segmentation algorithms. The patients come from a representative, institutional cohort, covering all stages (in terms of time from disease onset) and forms (relapsing-remitting, progressive) of MS. A 3D T1w and a 3D FLAIR sequence were acquired on a 3 Tesla Philips Achieva scanner. All 3D volumes feature $193x193x229$ voxels in 1mm isotropic resolution. The dataset divides into a fixed training set of 200, a validation set of 21, and a test set of 200 cases. The annotations feature a total of 4791 blobs, with 25.69 ± 23.01 blobs per sample. Expert neuroradiologists annotated the MS lesions manually and ensured pristine ground truth quality with consensus voting.

Procedure & Technicalities: For all training runs of 500 epochs, we set the initial learning rate to $1e-2$ and the batch size to 4. The networks are trained on a single GPU using 2 random crops with a patch size of $192x192x32$ voxels per batch element after applying a

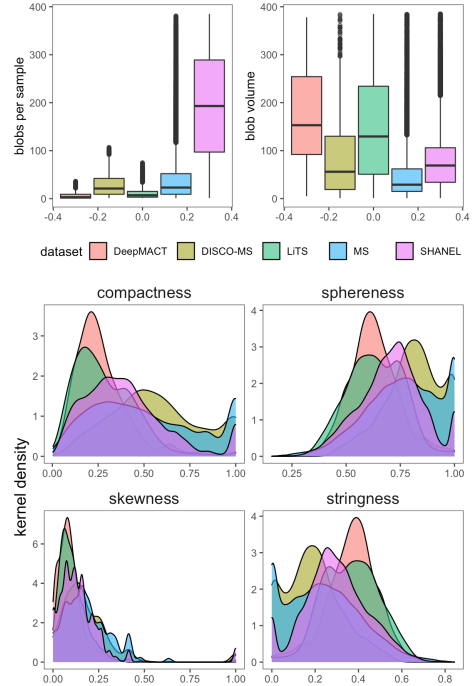


Fig. 4. Dataset heterogeneity and instance imbalance. Boxplot left: blob count per sample; Boxplot right: volume per blob. For visualization purposes, the boxplots are cut off at the 95% percentile. The four kernel density plots on the bottom depict four shape features, defined as: *Compactness*: Volume of blob divided by the volume of a hypothetical enclosing sphere. *Sphereness*: Ratio of the maximum distance within a blob to the diameter of a hypothetical sphere with the same volume as the blob. *Stringness*: Equals $1 - \text{Sphereness}$ and approaches 1 for string-like shapes. *Skewness*: Approaches 1 if a blob is thick or dense on one end and has a large tail on the other side.

min/max normalization. As the MS dataset comes with a predefined validation set of 21 images, we also save the checkpoint with the lowest loss on the validation set and compare it to the respective last checkpoint of the training. In addition to the standard *dice*, we also compare against *tversky*. Furthermore, we conduct an ablation study to find out how the performance metrics are affected by choosing different values for α and β .

3.2 Liver Tumors - LiTS (Thorax CT)

Dataset & Segmentation Task: To develop an understanding for *blob loss* performance on other imaging modalities, we train a model for segmenting liver tumors on CT images of the LiTS challenge [4]. The dataset consists of varying high-resolution CT images of the whole thorax. The challenge’s original task was segmenting liver and liver tumor tissue. As we are primarily interested in segmenting small fragmented structures, we limit our experiments to the liver area and segment only liver tumor tissue (in contrast to tumors, the liver represents a huge solid structure and we are interested in blobs). We split the publicly available training set into 104 images for training and 27 for testing. The annotations were created by expert radiologists and feature a total of 908 blobs, with 12.39 ± 14.92 blobs per sample.

Procedure & Technicalities: For all training runs of 500 epochs, we set the initial learning rate to $1e-2$ and the batch size to 2. The networks are trained on two GPUs in parallel using 2 random crops with a patch size of $192x192x64$ voxels per batch element. We apply normalization based on windowing on the Hounsfield (HU) scale. Therefore, we define a normalization window suitable for liver tumor segmentation around center 30 HU with a width of 150 HU, and 20% added tolerance.

3.3 DISCO-MS (light-sheet microscopy)

Dataset & Segmentation Task: To develop an understanding for *blob loss* performance on other imaging modalities, we train a model for segmenting Amyloid plaques in light-sheet microscopy images of the DISCO-MS dataset [3]. The volumes of $300x300x300$ voxels resolution contain cleared tissue of mouse brain. We split the publicly available dataset into 41 volumes for training and six for testing. The annotations feature a total of 988 blobs, with 28.32 ± 24.44 blobs per sample. Even though the label quality is very high, the results should still be interpreted with care following the guidelines in Section 2.5.

Procedure & Technicalities: For all training runs of 800 epochs, we set the initial learning rate to $1e-3$ and the batch size to 6. As our initial model trained with *dice* does not produce satisfactory results, we furthermore try learning rates of $1e-2$, $3e-4$ and $1e-4$, following the heuristics suggested by [1] without success. The networks are trained on two GPUs in parallel using 2 random crops with a patch size of $192x192x64$ per batch element. The images are globally normalized, using a minimum and maximum threshold defined by the 0.5 and 99.5 percentile.

3.4 SHANEL (light-sheet microscopy)

Dataset & Segmentation Task: For further validation, we evaluate on segmenting neurons in light-sheet microscopy images of the SHANEL dataset [31]. The volumes of $200x200x200$ voxels resolution contain cleared human brain tissue from the primary visual cortex, the primary sensory cortex, the primary motor cortex, and the hippocampus. We split this publicly available dataset into nine volumes for training and three for testing. The annotations feature a total of 20684 blobs, with 992.14 ± 689.39 blobs per sample. As the data is more sparsely annotated than DISCO-MS, F1 and especially DSC should be interpreted with great care, as described in Section 2.5.

Procedure & Technicalities: For all training runs of 1000 epochs, we set the initial learning rate to $1e-3$ and the batch size to 3. The networks are trained on two GPUs in parallel using 6 random crops with a patch size of $128x128x32$ per batch element, with min/max normalization.

3.5 DeepMACT (light-sheet microscopy)

Dataset & Segmentation Task: For further validation, we evaluate segmentation of micrometastasis in light-sheet microscopy images of the DeepMact dataset [20]. The volumes of $350x350x350$ resolution contain cleared tissue featuring different body parts of a mouse. We split the publicly available dataset into 115 images for training and 19 for testing. The annotations feature a total of 484 blobs, with 6.99 ± 8.14 blobs per sample. As the data is sparsely annotated, F1 and especially DSC should be interpreted with great care, as described in Section 2.5.

Procedure & Technicalities: For all training runs of 500 epochs, we set the initial learning rate to $1e-2$ and the batch size to 4. The networks are trained on a single GPU using 2 random crops with a patch size of $192x192x48$. The images are globally normalized based using a minimum and maximum threshold defined by the 0.0 and 99.5 percentile.

4 Results

Table 1 summarizes the results of our experiments. Across all datasets, we find that extending *dice* to a *blob loss* helps to improve detection metrics. Furthermore, in some cases, we also observe improvements to volumetric performance measures. This is also supported by the results from evaluating the best model checkpoint for the MS dataset, see supplemental materials. While model selection seems not beneficial on this dataset, employing *blob loss* produces more robust results, as both the *dice* and *tversky* models suffer performance drops for the *best* checkpoints. Notably, even though *tversky* was explicitly proposed for MS lesion segmentation, it is clearly outperformed by *dice*, as well as *blob dice* and *blob tversky*. Further, even with the mitigation strategies suggested by the authors, *inverse weighting* produced over-segmentations.

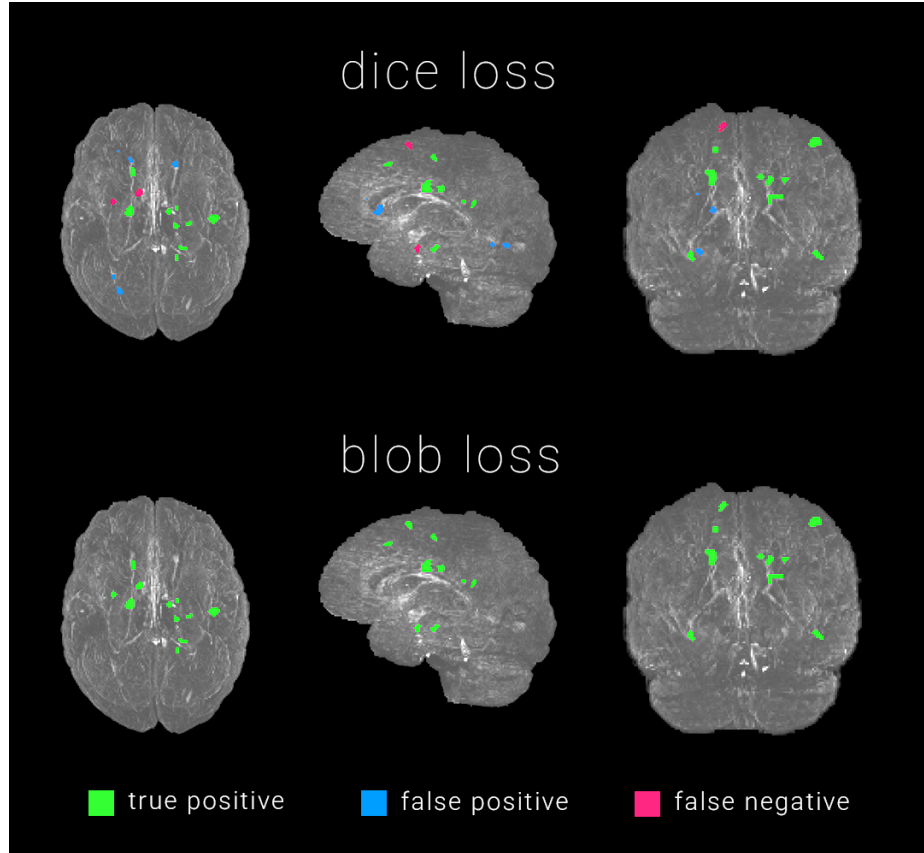


Fig. 5. Comparison of detection performance. Maximum intensity projections of the FLAIR images overlayed with segmentations for *dice* and *blob dice*. Lesions are colored according to their detection status: Green for *true positive*; Blue for *false positive*; Red for *false negative*. In this case, transformation to a *blob loss* improves $F1$ from 0.74 to 1.0. This is driven by an increase in *instance-sensitivity* from 0.83 to 1.0 and *instance-precision* from 0.67 to 1.0. Therefore, for this particular patient *blob loss* boosts $F1$ by simultaneously improving detection of foreground and suppression of background signal. This seems to be a regular pattern across multiple segmentation problems, compare Table 1. Refer to Figure 6 for a volumetric analysis.

Table 1. Experimental results for five datasets. For all training runs with *blob loss* we use $\alpha = 1$ and $\beta = 2$. Across all experiments extending *dice* to *blob dice* and *tversky* to *blob tversky* improves *F1* score. This improvement is always achieved by better suppression of the background signal. For LiTS, SHANEL and DeepMACT also *Instance Sensitivity* is improved. Furthermore, this is accompanied by an improvement in volumetric segmentation performance, namely DSC and Surface DSC. Note that the results for LiTS are based on a different, more challenging test set and are therefore not comparable with the public leaderboard of the LiTS challenge. For DISCO-MS, the *dice* model completely over-segments and produces dissatisfactory results. Therefore, we try two additional training runs with reduced learning rates following the heuristics suggested by [1], resulting in similar over-segmentation. The same problem is observed for *inverse weighting (iw)*. Shirokikh et al. [24] themselves note the stability problems of the method and suggest lowering the learning rate to $1 - e3$. However, following this approach improves volumetric- but leads to similar detection performance.

dataset	loss	lr	DSC	SDSC	F1	IS	IP
MS	blob dice	1e-2	0.680	0.848	0.810	0.822	0.828
	dice	1e-2	0.660	0.820	0.758	0.854	0.711
	iw [24]	1e-2	0.153	0.167	0.278	0.801	0.188
	iw [24]	1e-3	0.243	0.273	0.282	0.819	0.189
	blob tversky	1e-2	0.690	0.852	0.804	0.829	0.804
	tversky	1e-2	0.601	0.697	0.566	0.854	0.459
LiTS	blob dice	1e-2	0.663	0.542	0.657	0.861	0.631
	dice	1e-2	0.659	0.546	0.623	0.801	0.599
SHANEL	blob dice	1e-3	0.543	0.808	0.792	0.874	0.724
	dice	1e-3	0.539	0.794	0.783	0.854	0.723
DISCO-MS	blob dice	1e-3	0.546	0.678	0.589	0.760	0.481
	dice	1e-3	0.095	0.083	0.012	0.870	0.006
	dice	3e-4	0.016	0.036	0.379	0.896	0.240
	dice	1e-4	0.007	0.011	0.228	0.825	0.132
DeepMACT	blob dice	1e-2	0.357	0.393	0.391	0.871	0.276
	dice	1e-2	0.353	0.372	0.367	0.801	0.254

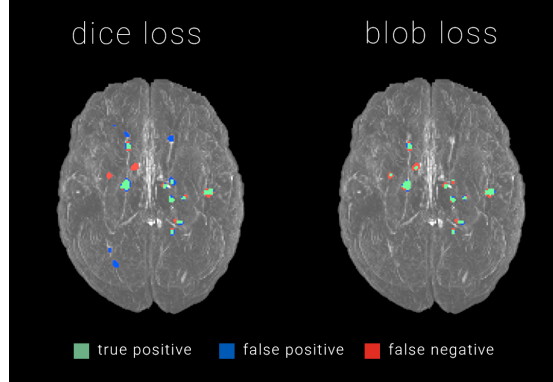


Fig. 6. Comparison of volumetric segmentation performance. Maximum intensity projections of the FLAIR images overlayed with segmentations for *dice* and *blob dice*. Lesions are colored according to their detection status: Green for *true positive*; Blue for *false positive*; Red for *false negative*. For this particular patient, applying the transformation to a *blob loss* improves the volumetric Dice coefficient from 0.56 to 0.70. This is caused by an increase in *volumetric precision* from 0.48 to 0.75, while the *volumetric sensitivity* remains constant at 0.66. Thus, unlike on the detection level, the improvement is solely reached due to better suppression of background signal, compare Figure 5.

Table 2. Ablation analysis on the *blob loss*' hyperparameters α and β for the MS lesions dataset. We observe that *blob loss* seems to be quite robust with regard to hyperparameter choice, as long as the global term remains present, compare Equation (2). The default parameters $\alpha = 2$ and $\beta = 1$ provide best results.

loss	α	β	DSC	S	P	SDSC	F1	IS	IP
blob dice	3	1	0.674	0.629	0.765	0.833	0.790	0.796	0.815
blob dice	2	1	0.680	0.626	0.782	0.848	0.810	0.822	0.828
blob dice	1	1	0.658	0.580	0.802	0.839	0.804	0.840	0.801
blob dice	1	2	0.630	0.552	0.803	0.819	0.792	0.832	0.786
dice	1	0	0.660	0.704	0.656	0.820	0.758	0.854	0.711
blob	0	1	0.522	0.409	0.837	0.728	0.744	0.805	0.727

Table 2 summarizes the results of the ablation study on α and β parameters of *blob loss*. We find that assigning higher importance to the global parameter, by choosing $\alpha = 2$ and $\beta = 1$ seems to produce the the best results. Overall, we find that *blob loss* seems quite robust regarding the choice of hyperparameters as long as the global term remains included by choosing a β greater than 0.

5 Discussion

Contribution: *blob loss* can be employed to provide existing loss functions with instance imbalance awareness. We demonstrate that the application of *blob loss* improves detection- and in some cases even volumetric segmentation performance across a diverse set of complex 3D bio-medical segmentation tasks. We evaluate *blob loss*' performance in the segmentation of multiple sclerosis (MS) lesions in MR, liver tumors in CT, and segmentation of different biological structures in 3D light-sheet microscopy datasets. Depending on the dataset, it achieves these improvements either due to better detection of foreground objects, better suppression of background objects, or both. We provide an implementation of *blob loss* leveraging on a precomputed connected component analysis for fast processing times.

Limitations: One disadvantage of *blob loss* compared to other loss functions is certainly its more extensive computational requirements. By definition, the user is required to run computations with large patch sizes that feature multiple instances. This results in an increased demand for GPU memory, especially when working with 3D data (as in our experiments). However, larger patch sizes have proven helpful for bio-medical segmentation problems in general [12]. Furthermore, according to our formulation, *blob loss* possesses an interesting mathematical property, it penalizes false positives proportionally to the number of instances in the volume. Additionally, even though *blob loss* can easily be reduced to a single hyperparameter, and it proved quite robust in our experiments, it might be sensitive to hyperparameter tuning. Moreover, by design *blob loss* can only improve performance for multi-instance segmentation problems.

Interpretation: One can only speculate why *blob loss* improves performance metrics. CNNs learn features that are very sensitive to texture [10]. Unlike conventional loss functions, *blob loss* adds attention to every single instance in the volume. Thus the network is forced to learn the instance imbalanced features such as, but not limited to morphology, and texture, which would not be well represented by optimizing via *dice* and alike. Such instance imbalance was observed in the medical field, as it has been shown that MS lesions change their imaging phenotype over time, with recent lesions looking significantly different to older ones [7]. These aspects might explain the gains in instance sensitivity. Furthermore, adding the multiple instance terms leads to heavy penalization on background, which might explain why we often observe an improvement in precision, see supplemental materials. Another interesting aspect is that *blob loss* seems to stabilize model training, as we obtain more robust results for our MS model selection study, the architecture ablation study, as well as the DISCO-MS experiment, see supplemental materials.

Outlook: Future research will have to reveal to which extent transformation to *blob loss* can be beneficial for other segmentation tasks and loss functions. A first and third place in recent public segmentation challenges using a compound-based variant *blob loss* indicate that *blob loss* might possess broad applicability towards other instance imbalanced semantic segmentation problems.

Acknowledgement

Bjoern Menze, Benedikt Wiestler and Florian Kofler are supported through the SFB 824, subproject B12.

Supported by Deutsche Forschungsgemeinschaft (DFG) through TUM International Graduate School of Science and Engineering (IGSSE), GSC 81.

Lucas Fidon, Suprosanna Shit and Ivan Ezhov are supported by the Translational Brain Imaging Training Network(TRABIT) under the European Union's 'Horizon 2020' research & innovation program (Grant agreement ID: 765148).

Ivan Ezhov, Suprosanna Shit are funded by DComEX (Grant agreement ID: 956201).

With the support of the Technical University of Munich – Institute for Advanced Study, funded by the German Excellence Initiative.

Supported by Anna Valentina Lioba Eleonora Claire Javid Mamasani.

Suprosanna Shit is supported by the Graduate School of Bioengineering, Technical University of Munich.

Jan Kirschke has received Grants from the ERC, DFG, BMBF and is Co-Founder of Bonescreen GmbH.

Bjoern Menze acknowledges support by the Helmut Horten Foundation.

Research reported in this publication was partly supported by AIME GPU cloud services.

6 Supplemental Materials

In the supplemental materials we use the acronyms introduced in the main text. For easier understanding we repeat the ones used in the tables: learning-rate (lr); Sørensen-Dice similarity coefficient (DSC); Surface Dice similarity coefficient (SDSC); Instance sensitivity (IS); Instance Precision (IP)

6.1 Data Availability Statements

As the MS dataset contains sensitive patient information, requests for the MS data will be reviewed by an ethical committee to determine whether the request is subject to any confidentiality obligations. Requests should contain a research proposal, an ethics statement, and a data transfer agreement.

LiTS challenge data is publicly available at codalab.org

SHANEL, DISCO-MS, and DeepMACT datasets are available upon request via discotechnologies.org

6.2 Why the two hyper-parameters α and β ?

One might wonder why *blob loss* is defined with α and β , while β could easily be defined as $1 - \alpha$. Assume one would want to extend a conventional soft dice loss (this equals $\alpha = 1$ and $\beta = 0$) to a *blob dice* with equal weights to see if it aids segmentation performance. In this case, α and β would both become 0.5. As the initial soft dice loss is now halved, one needs to double the learning rate to maintain comparability between training runs. These learning rate adjustments can become cumbersome, especially when operating with non equal weighted loss candidates.

6.3 Why do we need masking?

To explore the effect of the masking defined in Equation (1) we train another model on the MS dataset. Therefore, we keep all training parameters constant except for the loss. Here, we skip the masking inside the loss computation. We find that the masking is crucial for achieving a high segmentation performance, see Table 42.

Table 42. Segmentation performance when computing the loss without masking. The network tends to oversegment as reflected by the high instance sensitivity (IS) compared to the low instance precision (IP). The low performance is also reflected by the volumetric metrics DSC and SDSC.

dataset	architecture	loss	lr	DSC	SDSC	F1	IS	IP
MS	<i>BasicUnet</i>	blob dice	1e-2	0.680	0.848	0.810	0.822	0.828
MS	<i>BasicUnet</i>	dice	1e-2	0.660	0.820	0.758	0.854	0.711
MS	<i>BasicUnet</i>	no_masking	1e-2	0.358	0.382	0.297	0.829	0.201

6.4 MS model selection experiment

Table 43. Results for the model selection experiment on MS data. We evaluate the checkpoint with the lowest loss on the validation set of 21 patients. As *dice* and especially *tversky* suffer big performance drops, conducting model selection seems to hurt the networks’ generalization ability. Training with *blob loss* leads to more robust performance.

dataset	architecture	loss	DSC	SDSC	F1	IS	IP
MS	<i>BasicUnet</i>	blob dice	0.678	0.849	0.800	0.859	0.775
MS	<i>BasicUnet</i>	dice	0.640	0.800	0.759	0.810	0.748
MS	<i>BasicUnet</i>	blob tversky	0.692	0.857	0.796	0.848	0.775
MS	<i>BasicUnet</i>	tversky	0.405	0.461	0.413	0.851	0.302

6.5 Multi-class Segmentation Extension of *blob loss*

Extension to multi-class segmentation problems can be achieved by summing across the foreground classes. Let \mathcal{L} a loss function for binary segmentation, and let $\mathbf{p} = (p_i^c)_{i \in \Omega, c=0 \dots C}$ be the predicted segmentation and $\mathbf{g} = (g_i^c)_{i \in \Omega, c=0 \dots C}$ the one-hot encoding of the ground-truth segmentation, where Ω is the image domain and $C \geq 1$ is the number of foreground classes. We assume without loss of generality that the background corresponds to the class $c = 0$.

We propose to define the instance-aware loss function \mathcal{L}_{blob} associated with \mathcal{L} as

$$\mathcal{L}_{blob}(\mathbf{p}, \mathbf{g}) = \frac{1}{C} \sum_{c=1}^C \left(\frac{1}{N_c} \sum_{n=1}^{N_c} \mathcal{L}((p_i^c)_{i \in \Omega_{c,n}}, (g_i^c)_{i \in \Omega_{c,n}}) \right) \quad (3)$$

where $\Omega_{c,n}$ is the image domain after excluding the voxels labeled as c in the ground-truth segmentation, and that does not belong to the instance n .

The final loss for multi-class segmentation has the same form as for the binary segmentation case

$$\mathcal{L} = \alpha \mathcal{L}_{global} + \beta \mathcal{L}_{blob} \quad (4)$$

where $\alpha \geq 0$ and $\beta \geq 0$. Depending on the segmentation task at hand, one could further consider the introduction of class-specific α and β .

6.6 Dependency on Network architecture

U-Nets are the state-of-the-art architecture for bio-medical semantic segmentation [22]. As our primary goal is to evaluate a novel loss function, we choose the most standard U-Net architecture we could find for our experiments, see Figure 42. To investigate whether blob loss is dependent on the architecture we

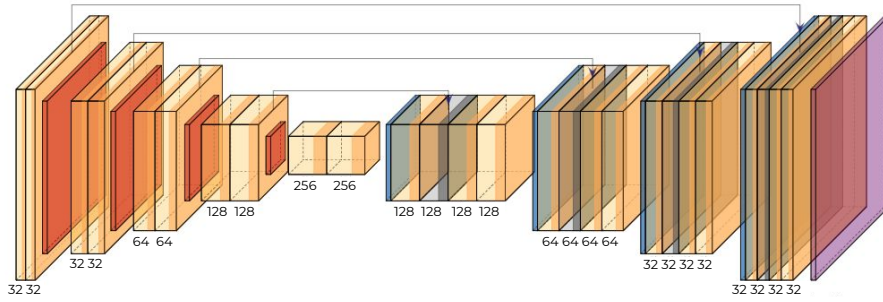


Fig. 42. The U-Net architecture used in the experiments, consisting of encoder and decoder parts. The numbers under the convolutional layers represent the channel count. The implementation is available via MONAI and is inspired by Falk et al. [8].

conduct a network architecture ablation study on the MS dataset. Despite exchanging the network architecture, we set the learning rate to $1e-3$ and keep the other parameters constant to the previous training runs. We compare a *blob dice* and *dice* baseline with *UNETR* [11]. Unlike our basic U-Net implementation *UNETR* features transformers. The implementation is available via MONAI. Table 44 summarizes the results of the model selection ablation study.

Table 44. Architecture ablation study. We compare *dice* against *blob dice* for training runs with *UNETR* [11]. The results indicate that the performance improvements of *blob loss* are architecture agnostic.

dataset	architecture	loss	lr	DSC	SDSC	F1	IS	IP
MS	<i>UNETR</i>	<i>dice</i>	1e-3	0.380	0.386	0.383	0.870	0.272
MS	<i>UNETR</i>	<i>blob dice</i>	1e-3	0.632	0.789	0.691	0.889	0.600

6.7 Increased Instance-wise Penalization of False Positives for Soft Dice Loss

Applying *blob loss* leads to increased instance-wise penalization of false positives. Let Y be the predicted segmentation, L be the ground-truth binary segmentation, and $N > 0$ the number of instances. Reasonably, we can assume that our ground truth is perfect and can be used for accurate false-positives and false-negatives categorization. Let $\{L_i\}_{i=1}^N$ be the masks of the binary instances. Hence, by construction we have $\sum_{i=1}^N L_i = L$. Further, we define the domain mask for each instance L_i as follows

$$\Omega_i = I - \sum_{j=1, j \neq i}^N L_j \quad (5)$$

where I is the mask on the image domain Ω with all its values equal to 1.

Although we predict all instances in a single channel, one can decompose it into $N + 1$ number of channel

$$Y = \sum_{i=1}^N L_i \odot Y + \left(I - \sum_{i=1}^N L_i \right) \odot Y \quad (6)$$

where \odot denotes Hadamard product. We denote $L_i \odot Y$ as Y_i and $(I - \sum_{i=1}^N L_i) \odot Y$ as Y_{fp} . Note that Y_i consists of voxel-wise true-positives and Y_{fp} consists of false-positives. Using the definition of the blob loss in Equation (1), with \mathcal{L} the soft Dice loss, $g = L_i$ and $p = Y \odot \Omega_i$

$$\begin{aligned} \mathcal{L}((p^j)_{j \in \Omega_i}, (g^j)_{j \in \Omega_i}) &= \frac{2 \times \sum_{j \in \Omega_i} g^j p^j}{\sum_{j \in \Omega_i} g_i^j + \sum_{j \in \Omega_i} p_i^j}; \text{ [superscript } j \text{ denotes each voxel]} \\ &= \frac{2 \times \sum_{j=1}^M L_i^j Y^j \Omega_i^j}{\sum_{j=1}^M L_i^j + \sum_{j=1}^M (Y^j \odot \Omega_i^j)} \\ &= \frac{2 \times \sum_{j=1}^M (L_i \odot Y)^j}{\sum_{j=1}^M L_i^j + \sum_{j=1}^M (Y \odot \Omega_i)^j}; \text{ [using the fact } L_i \odot \Omega_i = L_i] \end{aligned} \quad (7)$$

considering only $Y \odot \Omega_i$ we have

$$\begin{aligned}
Y \odot \Omega_i &= Y \odot \Omega_i \odot L_i + Y \odot \Omega_i \odot (I - L_i) \\
&= Y \odot L_i + Y \odot (I - \sum_{i=1, i \neq j}^N L_j) \odot (I - L_i) \\
&= Y \odot L_i + Y \odot (I - \sum_{i=1, i \neq j}^N L_j) - Y \odot L_i; \text{ [since } L_i \odot L_j = 0 \text{ for } i \neq j] \\
&= Y \odot L_i + Y \odot (I - \sum_{i=1}^N L_j) \\
&= \sum_{j=1}^M Y_i^j + \sum_{j=1}^M Y_{fp}^j
\end{aligned} \tag{8}$$

Replacing Eq. 8 in Eq. 7 we get

$$\mathcal{L}((p^j)_{j \in \Omega_i}, (g^j)_{j \in \Omega_i}) = \frac{2 \times \sum_{j=1}^M Y_i^j}{\sum_{j=1}^M L_i^j + \sum_{j=1}^M Y_i^j + \sum_{j=1}^M Y_{fp}^j} \tag{9}$$

The term $\sum_{j=1}^M Y_{fp}^j$ in the denominator penalizes the false positive and is present for every instance i . Therefore, the instance-aware soft Dice loss penalizes more the false positives than the soft Dice loss. Also note that the degree of false-positives penalty is proportional to the number of instances. This dynamic penalty is beneficial in preventing network from over-predicting in case of many instances while it does not affect much for fewer instances.

Bibliography

- [1] Bengio, Y.: Practical recommendations for gradient-based training of deep architectures (2012)
- [2] Berman, M., Triki, A.R., Blaschko, M.B.: The lovász-softmax loss: A tractable surrogate for the optimization of the intersection-over-union measure in neural networks. In: Proceedings of the IEEE Conference on Computer Vision and Pattern Recognition, pp. 4413–4421 (2018)
- [3] Bhatia, H., Brunner, A., Rong, Z., Mai, H., Thielert, M., Al-Maskari, R., Paetzold, J., Kofler, F., Todorov, M., Ali, M., et al.: Proteomics of spatially identified tissues in whole organs. arXiv (2021)
- [4] Bilic, P., Christ, P.F., Vorontsov, E., Chlebus, G., Chen, H., Dou, Q., Fu, C.W., Han, X., Heng, P.A., Hesser, J., Kadoury, S., Konopczynski, T., Le, M., Li, C., Li, X., Lipková, J., Lowengrub, J., Meine, H., Moltz, J.H., Pal, C., Piraud, M., Qi, X., Qi, J., Rempfler, M., Roth, K., Schenk, A., Sekuboina, A., Vorontsov, E., Zhou, P., Hülsemeyer, C., Beetz, M., Ettlinger, F., Gruen, F., Kaassis, G., Lohöfer, F., Braren, R., Holch, J., Hofmann, F., Sommer, W., Heinemann, V., Jacobs, C., Mamani, G.E.H., van Ginneken, B., Chartrand, G., Tang, A., Drozdal, M., Ben-Cohen, A., Klang, E., Amitai, M.M., Konen, E., Greenspan, H., Moreau, J., Hostettler, A., Soler, L., Vivanti, R., Szeskin, A., Lev-Cohain, N., Sosna, J., Joskowicz, L., Menze, B.H.: The liver tumor segmentation benchmark (lits) (2019)
- [5] Caicedo, J.C., Goodman, A., Karhohs, K.W., Cimini, B.A., Ackerman, J., Haghghi, M., Heng, C., Becker, T., Doan, M., McQuin, C., et al.: Nucleus segmentation across imaging experiments: the 2018 data science bowl. *Nature methods* **16**(12), 1247–1253 (2019)
- [6] Eelbode, T., Bertels, J., Berman, M., Vandermeulen, D., Maes, F., Bisschops, R., Blaschko, M.B.: Optimization for medical image segmentation: theory and practice when evaluating with dice score or jaccard index. *IEEE Transactions on Medical Imaging* **39**(11), 3679–3690 (2020)
- [7] Elliott, C., Wolinsky, J.S., Hauser, S.L., Kappos, L., Barkhof, F., Bernasconi, C., Wei, W., Belachew, S., Arnold, D.L.: Slowly expanding/evolving lesions as a magnetic resonance imaging marker of chronic active multiple sclerosis lesions. *Multiple Sclerosis Journal* **25**(14), 1915–1925 (2019)
- [8] Falk, T., Mai, D., Bensch, R., Çiçek, Ö., Abdulkadir, A., Marrakchi, Y., Böhm, A., Deubner, J., Jäckel, Z., Seiwald, K., et al.: U-net: deep learning for cell counting, detection, and morphometry. *Nature methods* **16**(1), 67–70 (2019)
- [9] Fidon, L., Li, W., Garcia-Peraza-Herrera, L.C., Ekanayake, J., Kitchen, N., Ourselin, S., Vercauteren, T.: Generalised wasserstein dice score for imbalanced multi-class segmentation using holistic convolutional networks. In: International MICCAI Brainlesion Workshop, pp. 64–76, Springer (2017)

- [10] Geirhos, R., Rubisch, P., Michaelis, C., Bethge, M., Wichmann, F.A., Brendel, W.: Imagenet-trained cnns are biased towards texture; increasing shape bias improves accuracy and robustness. arXiv preprint arXiv:1811.12231 (2018)
- [11] Hatamizadeh, A., Tang, Y., Nath, V., Yang, D., Myronenko, A., Landman, B., Roth, H.R., Xu, D.: Unetr: Transformers for 3d medical image segmentation. In: Proceedings of the IEEE/CVF Winter Conference on Applications of Computer Vision, pp. 574–584 (2022)
- [12] Isensee, F., Jaeger, P.F., Kohl, S.A., Petersen, J., Maier-Hein, K.H.: nnunet: a self-configuring method for deep learning-based biomedical image segmentation. *Nature methods* **18**(2), 203–211 (2021)
- [13] Isensee, F., Petersen, J., Kohl, S.A., Jäger, P.F., Maier-Hein, K.H.: nnu-net: Breaking the spell on successful medical image segmentation. arXiv preprint arXiv:1904.08128 **1**, 1–8 (2019)
- [14] Jungo, A., et al: pymia: A python package for data handling and evaluation in deep learning-based medical image analysis. *Computer methods and programs in biomedicine* **198**, 105796 (2021)
- [15] Kofler, F., Ezhov, I., Isensee, F., Balsiger, F., Berger, C., Koerner, M., Paetzold, J., Li, H., Shit, S., McKinley, R., Bakas, S., Zimmer, C., Ankerst, D., Kirschke, J., Wiestler, B., Menze, B.H.: Are we using appropriate segmentation metrics? identifying correlates of human expert perception for cnn training beyond rolling the dice coefficient (2021)
- [16] Lin, T.Y., Goyal, P., Girshick, R., He, K., Dollár, P.: Focal loss for dense object detection. In: Proceedings of the IEEE international conference on computer vision, pp. 2980–2988 (2017)
- [17] Ma, J., Chen, J., Ng, M., Huang, R., Li, Y., Li, C., Yang, X., Martel, A.L.: Loss odyssey in medical image segmentation. *Medical Image Analysis* p. 102035 (2021)
- [18] Milletari, F., Navab, N., Ahmadi, S.A.: V-net: Fully convolutional neural networks for volumetric medical image segmentation. In: 2016 fourth international conference on 3D vision (3DV), pp. 565–571, IEEE (2016)
- [19] Misra, D.: Mish: A self regularized non-monotonic neural activation function. arXiv preprint arXiv:1908.08681 (2019)
- [20] Pan, C., Schoppe, O., Parra-Damas, A., Cai, R., Todorov, M.I., Gondi, G., von Neubeck, B., Bögürçü-Seidel, N., Seidel, S., Sleiman, K., et al.: Deep learning reveals cancer metastasis and therapeutic antibody targeting in the entire body. *Cell* **179**(7), 1661–1676 (2019)
- [21] Rahman, M.A., Wang, Y.: Optimizing intersection-over-union in deep neural networks for image segmentation. In: International symposium on visual computing, pp. 234–244, Springer (2016)
- [22] Ronneberger, O., Fischer, P., Brox, T.: U-net: Convolutional networks for biomedical image segmentation. In: International Conference on Medical image computing and computer-assisted intervention, pp. 234–241, Springer (2015)
- [23] Salehi, S.S.M., Erdoganmus, D., Gholipour, A.: Tversky loss function for image segmentation using 3d fully convolutional deep networks. In: International

workshop on machine learning in medical imaging, pp. 379–387, Springer (2017)

[24] Shirokikh, B., Shevtsov, A., Kurnukov, A., Dalechina, A., Krivov, E., Kostjuchenko, V., Golanov, A., Belyaev, M.: Universal loss reweighting to balance lesion size inequality in 3d medical image segmentation. In: International Conference on Medical Image Computing and Computer-Assisted Intervention, pp. 523–532, Springer (2020)

[25] Shit, S., Paetzold, J.C., Sekuboyina, A., Ezhov, I., Unger, A., Zhylka, A., Pluim, J.P., Bauer, U., Menze, B.H.: cldice-a novel topology-preserving loss function for tubular structure segmentation. In: Proceedings of the IEEE/CVF Conference on Computer Vision and Pattern Recognition, pp. 16560–16569 (2021)

[26] Silversmith, W.: seung-lab/connected-components-3d: Zenodo Release v1. Zenodo (Sep 2021), <https://doi.org/10.5281/zenodo.5535251>, URL <https://doi.org/10.5281/zenodo.5535251>

[27] Sirinukunwattana, K., Snead, D.R., Rajpoot, N.M.: A stochastic polygons model for glandular structures in colon histology images. IEEE transactions on medical imaging **34**(11), 2366–2378 (2015)

[28] Sudre, C.H., Li, W., Vercauteren, T., Ourselin, S., Cardoso, M.J.: Generalised dice overlap as a deep learning loss function for highly unbalanced segmentations. In: Deep learning in medical image analysis and multimodal learning for clinical decision support, pp. 240–248, Springer (2017)

[29] Wright, L., Demeure, N.: Ranger21: a synergistic deep learning optimizer. arXiv preprint arXiv:2106.13731 (2021)

[30] Zhang, H., Zhang, J., Li, C., Sweeney, E.M., Spincemaille, P., Nguyen, T.D., Gauthier, S.A., Wang, Y.: All-net: Anatomical information lesion-wise loss function integrated into neural network for multiple sclerosis lesion segmentation. NeuroImage: Clinical p. 102854 (2021)

[31] Zhao, S., Todorov, M.I., Cai, R., Rami, A.M., Steinke, H., Kemter, E., Mai, H., Rong, Z., Warmer, M., Stanic, K., et al.: Cellular and molecular probing of intact human organs. Cell **180**(4), 796–812 (2020)

[32] Zhu, W., Huang, Y., Zeng, L., Chen, X., Liu, Y., Qian, Z., Du, N., Fan, W., Xie, X.: Anatomynet: deep learning for fast and fully automated whole-volume segmentation of head and neck anatomy. Medical physics **46**(2), 576–589 (2019)